Motion-enhancement Assisted Digital Image Correlation of Lithium-ion Batteries during Lithiation

Anmol Jnawali[1], Anand N. P. Radhakrishnan[1,‡], Matt D.R. Kok[1,2], Francesco Iacoviello[1], Daniel J.L. Brett[1,2], Paul R. Shearing[1,2,*]

1 Electrochemical Innovation Lab, Department of Chemical Engineering, UCL, London WC1E 7JE, U.K.

2 The Faraday Institution, Quad One, Harwell Science and Innovation Campus, Didcot, OX11 0RA, U.K.

Authors to whom all correspondence should be addressed – e-mail: *Paul R. Shearing: p.shearing@ucl.ac.uk; ‡Anand N.P. Radhakrishnan: anand.radhakrishnan@ucl.ac.uk

Abstract

For the first time, a motion enhancement and registration technique (MERt) – an advanced phase based motion enhancement method combined with an optical flow based digital image correlation process is used to investigate batteries. This, in combination with the non-invasive investigative nature of X-ray computed tomography, makes for a powerful tool to examine the mechanism behind (de)lithiation of Li-ion cells. Through MERt, which magnifies the displacement of electrodes and tracks any internal changes, it is generally observed that the electrode expands outwards, but once encountering the solid barrier that is the cell casing, the electrode has nowhere to expand but inwards, which is why the electrode deformations initiate at the cell core. The technique clearly affirms that the greatest movement of electrodes during lithiation occurs at pre-existing inflection points in the jelly roll, which are a result of the manufacturing process, which eventually leads to the large deformations observed in this and previous works. MERt also indicates a contortion of the cell casings during lithiation which may be caused by the uneven expansion of the electrodes, but requires further studies to confirm.

Keywords

Lithium-ion battery; Motion enhancement; Image registration; Optical flow; Virtual unrolling; Lithiation

1. Introduction

Lithium-ion (Li-ion) cells have many characteristics which make them desirable for use in electric vehicles (EVs), such as high power and energy density, high capacity, and long cycle life. However, in the EV industry, once cells reach 80% of their original capacity, they are generally considered to be at their end-of-life (EOL). Therefore, investigating the mechanisms behind the decrease in capacity of cells due to ageing is imperative in order to maximise cell lifetime and improve cell design.

As spiral wound cells undergo ageing, the electrode coils eventually deform, causing cracks to appear on the electrode surface and loss of contact with the current collector, leading to an irreversible loss of capacity [1]. Kok *et al*. [2] have determined that the deformation of the jelly rolls occur at '*pre-existing inflection points*', which are

sites of structural weaknesses that arise during the rolling process during manufacturing. However, the mechanisms behind the deformation have not been clearly elucidated yet.

The intercalation and de-intercalation of lithium ions during cycling causes particle strain in the electrodes due to the associated volume expansions, this corresponds to around 10% and 300% in graphite [3] and silicon [4] anodes, respectively. Even the cathodes undergo volume expansions of around 4.5% for $LiNiCoAlO_2$ (NCA) [5], and 7.2% for $LiNiMnCoO_2$ (NMC) [6], respectively. The stresses related to these volume expansions cause cracking of the electrode particles: for example, Markervich *et al*. [7] identified micro- and nano-scale cracks in graphite crystals using scanning electron microscopy; and Liu *et al*. [8] validated long term capacity loss in their experimental cell caused by cracking of NCA particles using X-ray CT.

Digital volume correlation (DVC) and digital image correlation (DIC) are techniques used to measure displacement of matter within a sequence of volume or image data. Tomographic imaging has allowed researchers to obtain vastly greater knowledge of the complex microstructure of battery materials. Furthermore, recent advances in X-ray technology has allowed researchers to obtain three-dimensional (3D) volume data at increasingly higher resolutions and at faster rates in laboratory conditions [9]. DIC/DVC combined with the non-invasive nature of X-ray computed tomography (CT) makes for an effective technique to track and quantify changes over time. Eastwood *et al*. [10] used laboratory X-ray CT coupled with DVC to demonstrate the uneven dilation caused by lithiation in a manganese oxide electrode, and Finegan *et al*. [11] were able to employ a synchrotron X-ray source to track swelling and local displacement in the electrodes caused by lithiation in real time.

From previous works [2] it was shown that deformation of the jelly roll in cylindrical cells occurs as a function of ageing, and that it initiates at specific pre-determined points. It is believed that the lithiation/delithiation mechanism plays a part in the progression of the deformation. Here we attempt to decouple the effects of (de)lithiation on the eventual deformation of the jelly roll in cylindrical cells by combining a motion enhancement technique with image registration to accentuate the motion during lithiation at the pixel level. One such DIC technique for image registration is *'optical flow'*, which indicates the apparent movement of objects in images. It operates by tracking the velocity distribution of brightness, intensity, or patterns in image sequences [12]. To the authors' knowledge, the combination of a motion magnification followed by the analysis of the changes in internal cell structure using an optical flow based image registration is demonstrated here, for the first time.

2. Methodology

Five cells of varying geometries and differing internal structures were selected for this study, as seen in Figure 1. The cells selected were at different points in cycling, with varying degrees of structural deformations of the electrodes in order to include a range of electrode behavioural patterns caused by the severity of the deformations. Information on the selected cell models can be viewed in Table 1.

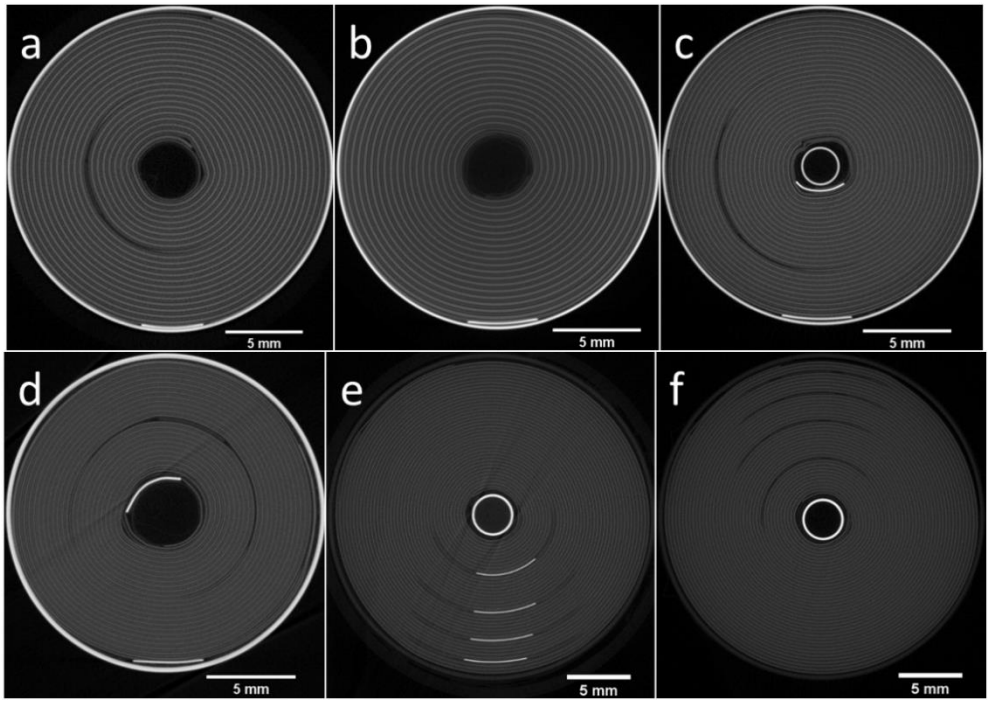

Figure 1: Cross-sectional (xy) slices of (a) M50; (b) MJ1; (c) VTC6; (d) HB6; (e-f) negative and positive ends of a Lithium Ion Power Cell, respectively.

Table 1: Information on the different cell types used in this study.

Model	Manufacturer	Chemistry	Geometry	Nominal Capacity (Ah)	Voltage Window (V)	# of cycles
M50	LG Chem.	Si/C / NMC	21700	5	2.5 – 4.2	1145
MJ1	LG Chem.	Si/C / NMC	18650	3.5	2.5 – 4.2	597
VTC6	Sony	C / NMC	18650	3.12	2.5 – 4.2	108
HB6	LG Chem.	C / NMC	18650	1.5	2 – 4.2	150
Lithium Ion Power Cell (LPC)	LithiumWerks	C / LFP	26650	2.6	2 – 3.6	163

a) Cell Cycling & X-ray Computed Tomography

The selected cells were discharged to their lower cut-off voltage using discharge steps with increasingly lower C-rates using a Maccor Model 4200 and Bio-Logic SAS BCS-815. The cells were then charged to their upper

cut-off voltage in four charge steps using a Gamry potentiostat (Gamry Instruments, Warminster, USA). They were all charged at 1 A, tapering the current to 100 mA with a CV step cut-off limit of 45 minutes. The voltage profiles during charging of the cells can be found in *Figure A2* in the *Supplementary Information (SI)*. At every charge step, the cell underwent an *in situ* X-ray computed tomography (CT) scan around a region of interest in the cell using a Nikon XT H 225 (Nikon Metrology, Tring, UK) instrument. The aim was to maximise resolution, therefore half-length scans were carried out, instead of full cell scans, and the region of interest was selected to be at the centre of the cell in terms of height and width, thus the scans were truncated (a portion of the positive and negative terminals were not included in the field of view). Thus, pixel resolutions of 13-14 µm were achieved for the 21700 cells, and 13 µm and 16 µm for 18650 and 26650 cells, respectively. Utilising an exposure time of 0.5 s and beam energy and current of 190-195 kV and 250-260 µA, respectively, approximately 3100 projections were acquired for the 21700s. Similarly, the settings used for the 18650s were 0.5 s, 190 kV, 210-220 µA, and the settings for the 26650s were 0.5 s, 190 kV, 200 µA. The tomograms were then reconstructed using a filtered back projection algorithm (CT Pro 3D, Nikon Metrology).

A single slice from the scans at each charge step were taken from the same *z*-location (using the ends of the current collecting tabs as reference) in each cell, which formed sequential frames of the lithiation process. Table 2 provides some information on the voltage steps used for the various cells in this study. Automatic alignment of the stack of five slices from the different scans for each cell was carried out using the *"Align Slices"* module on Avizo (Version 9.5, Thermo Fisher Scientific). Due to the internal changes and also changes in the shape of the outer cell casing (as discussed in the *Results* section) during lithiation, the slice registration carried out by the automated process was may cause minor artefacts to be introduced in the subsequent analysis. Proper alignment is crucial, as the cell may shift in the holder slightly in-between the charge steps due to user interference, as such the development of an alignment tool more robust than the automatic alignment module is of interest in the future. The contrast between the frames from the different scans were normalised, and the frames were turned into a time lapse image sequence using Fiji (a distribution of ImageJ [13]). The resultant time-lapse video was exported from Fiji and are shown in *SI_Video_1[…]* – *SI_Video_5[…]* for the pristine cells and *SI_Video_11[…]* – *SI_Video_15[…]* for the cycled cells in the *SI*.

Table 2: Information on the voltage steps used for the in-situ scans for the different cells, where V1 and V5 are the lower and upper manufacturer's voltage cut-off limits, respectively.

Voltage Steps (V)	M50	MJ1	VTC6	HB6	LPC
V_1	2.5	2.5	2.5	2.0	2.0
V_2	3.3	3.3	3.3	3.3	3.0
V_3	3.6	3.6	3.6	3.6	3.2
V_4	3.9	3.9	3.9	3.9	3.4
V_5	4.2	4.2	4.2	4.2	3.6

b) Phase-based Video Magnification

The first step in the motion enhancement and registration technique (MERt) is to amplify the displacement of the electrodes using an established video magnification process. Video magnification was carried out using the phase-based Eulerian motion processing as detailed in the paper by Wadha *et al.* [14]. The technique translates noise instead of amplifying it as in previous iterations of the techniques [15]. In simplified terms, the motion magnification is based on complex-valued steerable pyramids, where the local phase over time is calculated. These phases are then band passed to isolate temporal frequencies, which correspond to the motion in the various spatial scales and orientations. The movement is magnified by multiplying the band passed phases with a factor, $1+\alpha$. The phase coefficients in each frame are then modified by this amount ($1+\alpha$) to enhance the motions in the video within a maximum bounds, estimated from a Gaussian kernel of width = σ. For example, a similar technique has been applied to amplify and track the breathing patterns of infants from low resolution video information; this is the first time to our knowledge that it has been applied to time-lapse X-ray data. The magnified videos are shown in *SI_Video_6[…] – SI_Video_10[…]* for the pristine cells and *SI_Video_16[…] – SI_Video_20[…]* for the cycled cells in the *SI*. The MATLAB script for the video magnification was used as published by the authors (Wadha *et al.* [14]), with some changes in the processing variables: the frequency cut-offs, alpha (α) and the spatial smoothing factor, sigma (σ). The code was executed on MATLAB (version R2018a). A narrower frequency band ensures a more focused amplification and a lesser amplification of noise, but it also carries with it a risk of overlooking physical phenomenon. This step, therefore, requires a rigorous user supervision, where a combination of a range of α and σ values needs to be tested.

c) TV-L – based Image Registration (Optical Flow)

The second step in MERt is to perform an '*optical flow*' DIC technique to the motion-amplified videos, where each frame represented a different (de)lithiation state. Optical flow was used to elucidate the global motion of the

electrodes in the magnified video at a pixel level. The process compares two frames at a time, using the first frame as reference, in order to generate movement vectors and flow fields based on pixel level changes. Movement is identified by the changes in the greyscale values of the pixels over small sub-areas in the frames. The optical flow image registration script was written on Python 3.7 using the total variation (TV) regularisation and L^1 norm algorithm as available on the Scikit-image package [16]. The TV-L optical flow method is known to be more resistant to noise and permits discontinuities in the flow field [17]–[19].

For accurate pixel registration, a well-defined cross-section of the images was required. It was particularly challenging to register pixels between cell-charging steps. For a video loaded on the Python script, a marching-squares based, contour-finding algorithm was used to find the edges of the cell-casing from the last frame of the video [20], commonly applied to find perimeters of well-defined features in images without affecting feature morphology [21]. Any background pixel values outside the cell-casing were ignored from analysis. The coordinates of the cell-casing from the last frame (after fully charging) was applied on all subsequent frames. This was crucial to ensure that the image registration step captured the overall bulging of the cell upon cycling. After 'masking' the background pixels in every frame in the video (as example masked frame shown in *Figure A1a* in *SI*), a Sobel edge-detection step [22] was used to pick-up the interfaces between the electrodes and the electrolyte. The edge-detection step amplifies the texture of each frame, highlighting the boundaries of each material in a Li-ion cell that subsequently act as 'seeds' for the optical flow image registration step – an example Sobel filtered frame is shown in *Figure A1b* in *SI*.

For a video of N frames, where each frame has a width of X pixels and a height of Y pixels, the optical flow for each frame is then calculated using the TV-L methodology. For a given frame, i, where $0 \leq i \leq N$, a displacement vector (u, v), also known as the disparity map, is calculated for each pixel at location (x, y), such that

$$image_i(x + u, y + v) = image_0(x, y) \quad (1)$$

where, $0 \leq x \leq X$ and $0 \leq y \leq Y$, and $image_0$ ($i = 0$) is the first frame of the video. The (u, v) vector field represents the Euclidean distance map between two pixels identified as similar between the two frames based on their pixel intensities. From the horizontal and vertical displacement vectors, (u, v), the total displacement magnitude was calculated from the square root of their squared sums, $\sqrt{(u^2 + v^2)}$. The total displacement magnitude was then plotted as a colour map overlaid on the corresponding frames. The colour map scaled from purple to yellow, where purple indicates no displacement, $\sqrt{(u^2 + v^2)} = 0$, and yellow denotes the maximum displacement, which is a scaled factor of the original pixel intensities. To show the direction of displacements, the (u, v) vector field have been

plotted as a 2D field of arrows, where the length of the arrows is the displacement magnitude (normalised by the largest magnitude to aid visualisation). The base of the arrows are at (x, y) and point towards ($x+u$, $y+v$).

d) Virtual Unrolling

The theory behind the virtual unrolling (VU) technique and its interpretation is presented by Kok *et al*.[2], and a simplified description is provided in this work. In order to find and resolve the contour in the acquisition of the cylindrical cells obtained through X-ray CT, image and edge enhancing techniques are applied. Firstly, the images have their grayscale re-scaled from 0 to 1, and the edge of the casing is determined by locating the longest contour with a grey-scale threshold within a certain range. The cell casing is highly attenuating and circular in cross section, so it provides an apt starting point for locating the centre of the cell, which is extracted by algorithmically trying all possible options for the centre and identifying the one that results in minimum casing distortion. Edge enhancement is carried out by applying a small kernel median filter and an unsharp mask. Consequently, the boundary between the cathode and anode provides the highest contrast and is suitable to be the edge of the repeating layer for unrolling. The jelly roll is extracted by finding the longest continuous contour and applying a coordinate system transform on the Cartesian data to obtain the cylindrical coordinates.

3. Results

3.1 Motion enhancement and Registration technique (MERt)

The Motion enhancement and Registration technique (MERt) is the combination of the individual techniques: video motion enhancement and the optical flow image registration. Video motion magnification is utilised because the optical flow technique on its own is not able to precisely identify minor electrode displacements. The motion enhancement amplifies both the small and large vectors, resulting in more distinct flow fields as well as aiding in the visual presentation of the effects of lithiation, such as shifts in electrodes and casing deformation.

For the figures produced by MERt presented in this work, the arrows represent flow vectors, indicating the direction and intensity (through its size) of the movement of battery materials, and the colour map represents the displacement magnitude, with a brighter, yellow colour representing greater movement and a darker, blue colour representing no movement: the *'dead zone'*. For the analysis of Li-ion batteries using this combined technique, cells with various geometries and internal structures were selected for this study in order to elucidate the effects of the anatomy of the cells, such as the internal current collecting tabs and pre-existing points of inflection on the jelly roll, on the shift of the electrodes during lithiation. It was previously determined that all cylindrical cells

contain, to varying degrees, an inflection point in the jelly roll (as an artefact of the manufacturing process) that provides a point of weakness for the propagation of deformation [2].

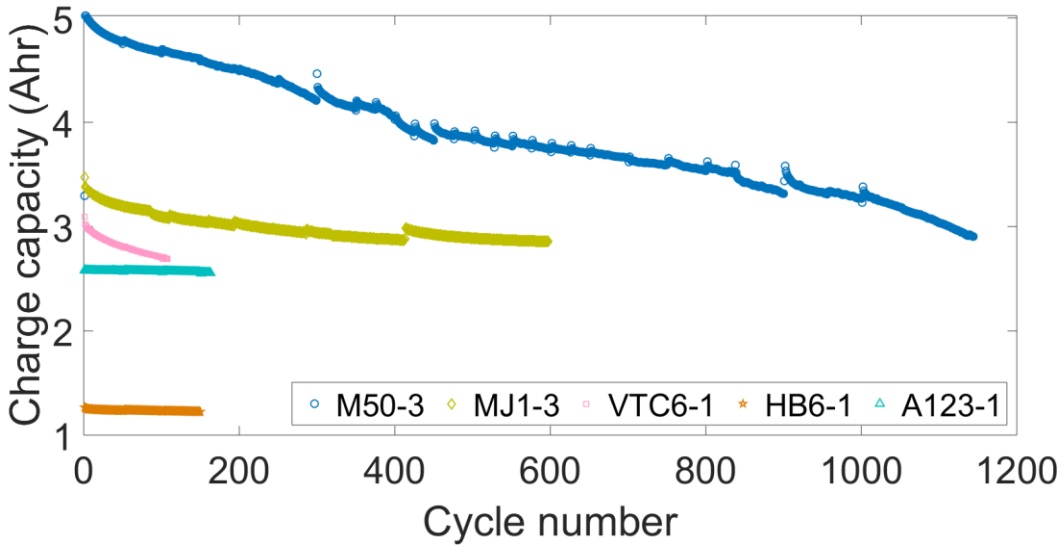

Figure 2: Charge capacities of the five cells used in this study.

The capacity fade profiles of the five cells used in this study can be found in Figure 2. It is seen that for the individually varying periods of cycling life shown in this figure, M50, MJ1, and VTC6 exhibit a greater rate of capacity fade compared to the HB6 and LPC cells. It is also observed that those very cells (M50, MJ1, and VTC6) showed to varying degrees, deformations in their jelly rolls, as opposed to the HB6 and LPC cells which showed virtually no deformations as shown in the reference images in Figure 3–Figure 7. MERt is carried out on the pristine cells, henceforth denoted by *P* preceded by the cell model. Figure 3 shows the flow fields of the pristine M50 and MJ1 cells. The flow fields are generated by comparing the frames of the video as a pair, with the first frame as the reference frame. The flow fields for the voltage step V_2 is created by using the frame at V_1 as reference, and V_3 vs. V_1, and so on. When looking at the evolution of the flow fields for M50-*P* in Figure 3b-e, it is informative to orient the image relative to compass points, where initially there is a flow of movement from east to west. As seen from Figure 3a there is empty space on the west side of the M50-*P* where the cathode electrode roll ends, providing space for the expansion of the electrodes. There is also movement of material towards the hollow core of the cell around the location where failure is predicted to occur by virtual unrolling as discussed below. On the west side, the electrode expands outwards, towards the cell casing. Then, from V_2, the dead zone towards the north-west starts to exert pressure inwards. At V_3 the pattern remains the same, but the movement becomes more concentrated towards the inflection point. By the end (V_4), the flow pattern on the west

also changes to an inwards flow. Throughout the whole lithiation process, there is greater pressure exerted on the inflection point than elsewhere, clearly elucidating one of the causes of the deformations as a result of cell cycling.

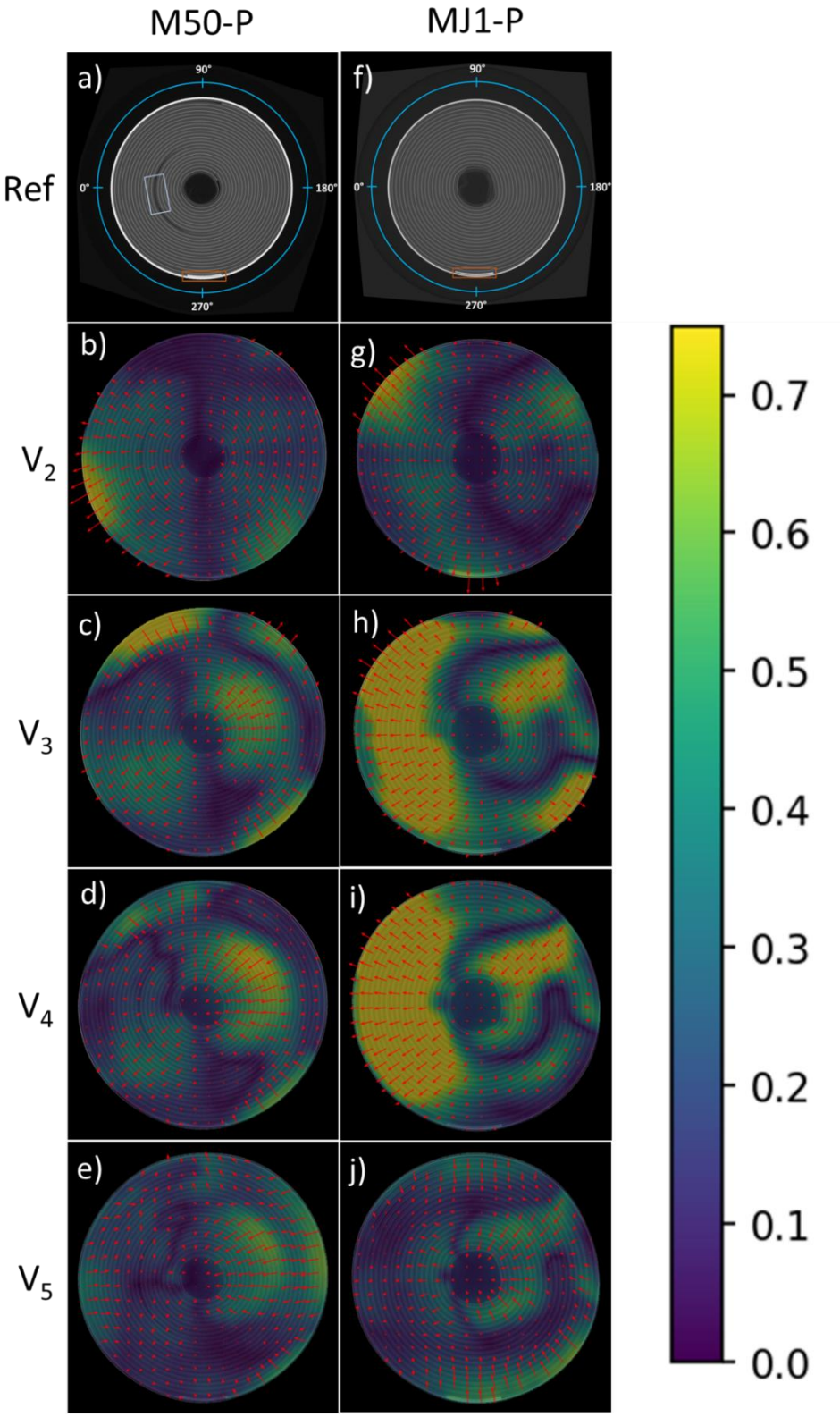

Figure 3: MERt of the pristine cells, (a-e) M50-P, (f-j) MJ1-P. A light-blue box is used to highlight positive current collecting tabs, and a bronze box is used to highlight negative current collecting tabs in the reference images.

Similar to the M50-*P*, the MJ1-*P* also demonstrates the exertion of pressure at the inflection point, however, it also shows a greater outwards movement on the left hand side. One possible reason for this could be that the MJ1 lacks an inner current collecting tab, which the M50 has (as highlighted by the pale box in Figure 3a). The welded inner tab (in the M50) may be acting as a barrier, decreasing the outwards displacement.

Part of the reason for the change in direction around the edge of the cell as the voltage increases could be that the electrodes expand in any direction where there is space as they are lithiated, but once they encounter the barrier that is the cell casing, they are forced to start expanding inwards, towards the hollow core. Another reason is that the cell casing seems to be contorting as lithiation occurs, which the MERt identifies. This may be caused by the pressure exerted by the uneven expansion of the electrode material inside the casing. The contortion of the cell casing of both M50-*P* and MJ1-*P* is more clearly visible in the enhanced videos provided in *SI* (*Figure A2* and *Figure A4*).

MERt is conducted on aged cells of the same model as the pristine batch, henceforth denoted by *C* preceded by the cell model. Figure 4b-e shows the flow fields of M50-*C*, a cell which had previously gone through 1144 cycles. The cell contains two deformations at the central core at opposing sides of the cell (Figure 4a). Unlike the M50-*P*, the flow sections are more evenly divided in M50-*C*. Initially there is more dead space in the centre, with outwards expansion, which then evolves into a partition of inwards compression segregated by a warped ring of dead zone from the outwards expansion zone. This pattern continues until V_5 where the movement in the outer expansion zone generally subsides and the movement at the centre of the cell continues to concentrate. Interestingly, the central flow fields are concentrated between the two deformations, more than at the deformations themselves.

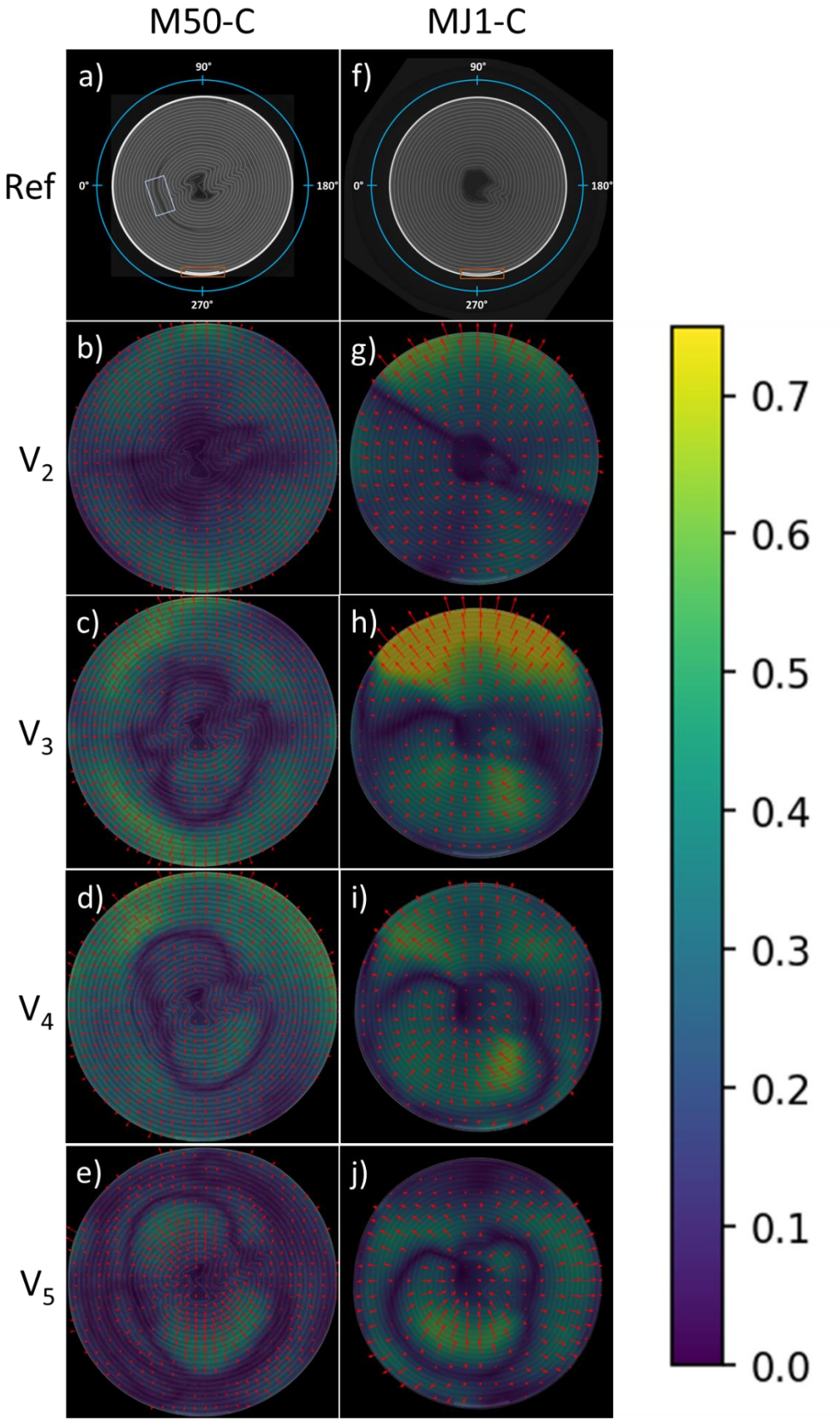

Figure 4: MERt of the cycled cells, (a-e) M50-C, (f-j) MJ1-C. A light-blue box is used to highlight positive current collecting tabs, and a bronze box is used to highlight negative current collecting tabs in the reference images.

The MJ1-*C*, which had undergone 597 cycles, also shows two different flow fields partitioned by a diagonal line of dead zone as seen in Figure 4g-j. The outwards movement observed at the top of the cell and around the edges is due to the deformation of the cell casing. At V_4, the formation of a concentrated ring of movement towards the centre of the cell separated by a ring of dead zone can be observed. The cell contains one electrode deformation, and once again, it can be seen that the movement is concentrated adjacent to the deformation, more than directly at the deformation. This suggests that initially, the nucleation point of the deformation and the concentration of electrode movement occurs at the inflection point, and as deformation reaches a critical point, the nucleation point shifts, contributing to the widening and expansion of the deformation.

The behaviour exhibited by the cell casing might have an impact on the movement of the electrodes as well: as one side of the casing compresses, limiting expansion of electrode in that direction, another side would expand, providing space for expansion. It is unclear as to the exact cause of the casing deformation, but from the magnified videos, it would seem the MJ1 is more prone this behaviour than the M50. It would be of interest to determine whether the casing deformation always takes a consistent pattern or whether it varies per cycle to more clearly determine whether it would have an effect on electrode movement, hence deformation. Willenberg *et al*. [23] were able to prove a change in the cell casing diameter of an 18650 Li-ion cell of around 10 µm using strain gauges. Furthermore, they also showed that the diameter change was non-linear during charge and discharge, which indicates that the casing might be deforming unevenly. This behaviour might also be the build-up of gases and not just the expansion/displacement of electrodes.

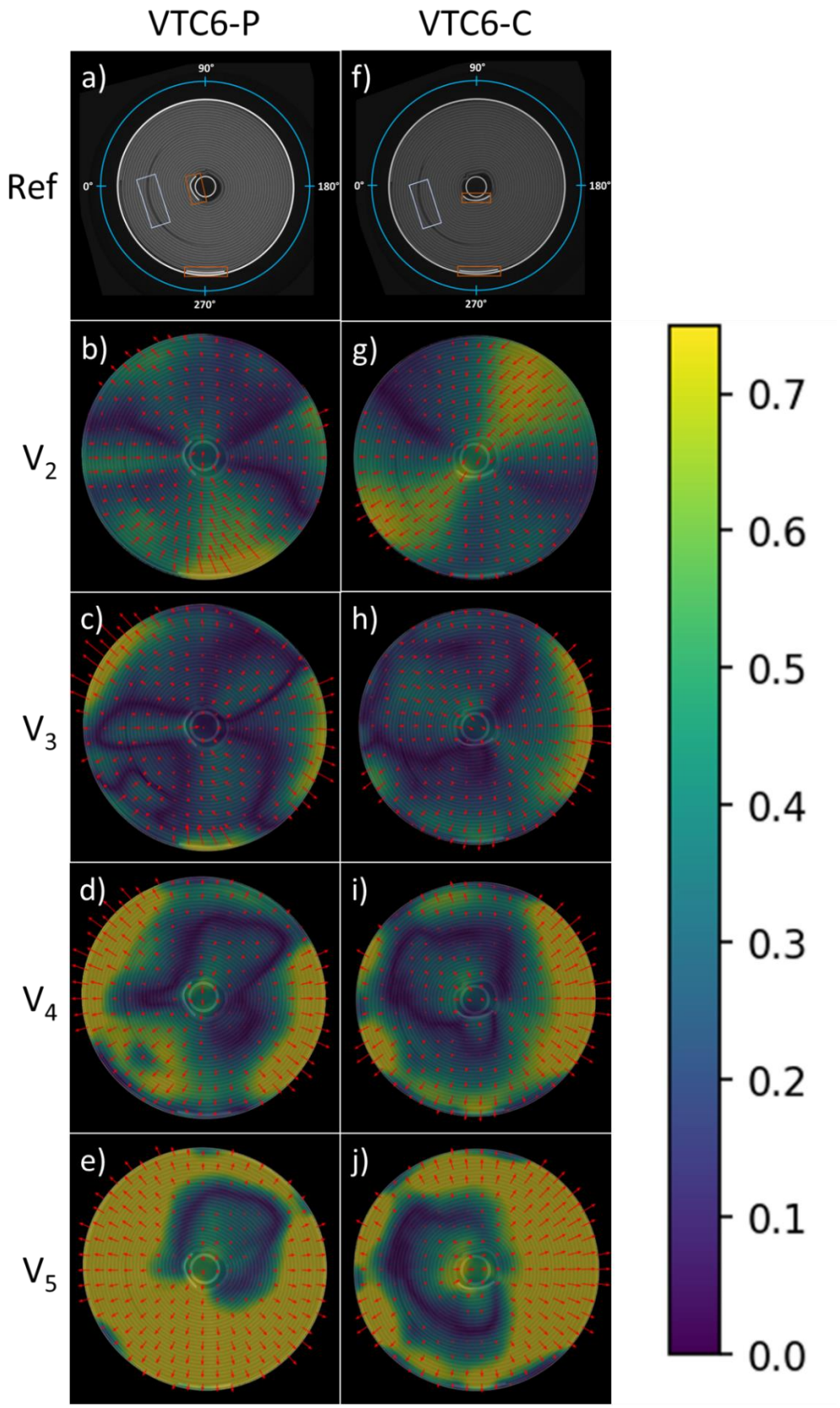

Figure 5: MERt of the pristine and cycled VTC6 cells, (a-e) VTC6-P, (f-j) VTC6-C. A light-blue box is used to highlight positive current collecting tabs, and a bronze box is used to highlight negative current collecting tabs in the reference image

The VTC6 cell contains a mandrel as can be seen in Figure 5. This is believed to supress the deformation of electrodes by acting as a support and limiting the space available for the deformation to occur [1]. It also contains two negative current collecting tabs, one at the edge of the cell casing and one at the centre of the cell. Initially, during charge, the pristine cell shows a flow of electrode movement from the south to the centre of the cell, and slight outward movements towards the east and north-west. Around V_4, this dynamic changes to show a greater shift of electrode towards the cell casing in all directions and also a less concentrated movement of electrode in the inner core towards the mandrel. This inner movement is occurring at a visible, pre-existing inflection point in the jelly roll as observed next to the inner negative tab in Figure 5a. This behaviour gets exacerbated as the voltage increases to V_5. Another feature in the flow field of the pristine VTC6 cell is that, in the initial few stages, there is pressure exerted by the electrodes directly towards the inner negative current collecting tab. As previously mentioned, the tab is welded and cannot move, so it is very likely that it is supressing some of the pressure that might have resulted in jelly roll deformation. The first thing that can be noticed when looking at the cycled VTC6 cell in Figure 5g-j, is that the location of the inner negative current collecting tab is different to the pristine cell. This has resulted in the formation of the deformation in a different location to the inflection observed in the pristine cell, and a difference in the movement of the electrodes. It can also be observed, that as the inflection point is located further from the inner negative tab, the pressure exerted by the electrodes reaches a higher intensity. This change also seems to have led to an initial flow field similar to that observed in MJ1-*C*. It can be seen that initially the electrodes flow in one direction, however, after reaching 3.6 V, the inwards movement of electrodes is concentrated at the deformation, and an outwards expansion surrounds the zone of inwards compression. This behaviour continues for the duration of the charge cycle, increasing in intensity. The intensity of the outwards expansion is lower towards the south and west, perhaps due to the influence of the positive and inner negative tabs.

The HB6 cells also contain two negative tabs and one positive tab, but no mandrel at the centre. Also, the location of the tabs are different to the VTC6 cells. The flow fields of the pristine HB6 cell in Figure 6b-e shows a generally one directional flow of electrode materials. Initially, the electrodes seem to be experiencing both tensile and compressive forces from east to west around the inner negative tab, with minimal forces in the direction of the tab itself. Similarly, the outer negative tab doesn't experience much force. As the voltage increases, the expansive forces seem to be greater, and they continue to increase, now applying forces on the negative tabs as the electrodes expand towards the empty spaces between the electrode roll and the cell casing. The cycled HB6 cell in Figure 6g-j shows a similar one directional trend, however, the compressive and expansive forces are moving from west

to east. One reason for this could be the big difference in the location of the inner negative and positive tabs between the pristine and cycled cells. The dead zones between the two cells are roughly mirrored, and once again, the expansive forces seem to increase as the voltage increases.

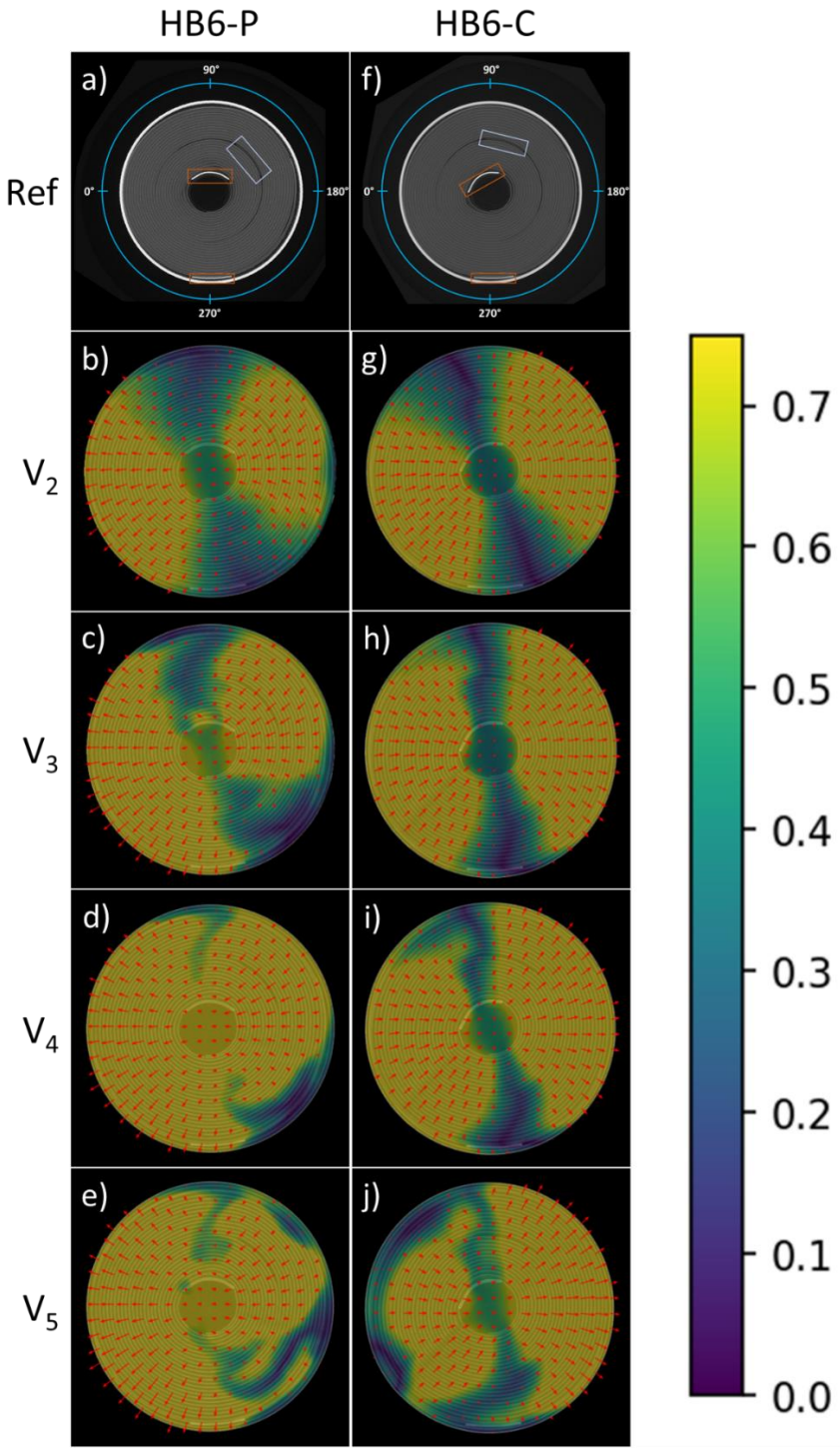

Figure 6: MERt of the pristine and cycled HB6 cells, (a-e) HB6-P, (f-j) HB6-C. A light-blue box is used to highlight positive current collecting tabs, and a bronze box is used to highlight negative current collecting tabs in the reference images.

Although the LPC cells contain positive and negative current collecting tabs at either ends of the tabs, they do not extend to the region of interest at the centre of the cell. The electrode displacement is expected to be different at different heights, partly due to the change in internal structure of the cell, and as such there is likely to be a vertical strain gradient. The investigation of the strain gradient along the z-axis may be of interest in future works. The only feature, or obstacle, present throughout the cell is the Mandrel. The LPC cell provides a glimpse into how a cell might behave during lithiation if it didn't contain any physical barriers amongst the jelly roll, such as current collecting tabs. Figure 7 shows the flow fields for the pristine and cycled LPC cell, which contains a mandrel and current collecting tabs at the positive and negative ends of the cell, but no tabs in the mid-section of the cell. It can be seen that without physical barriers in place, the electrodes simply shift in one direction. It is hard to say whether this is beneficial for the cycle life of the cell, however, after 163 cycles, the LPC cell has not shown any visible deformations, and as seen in Figure 2, its rate of capacity fade is low. The crystalline lattice volume change in LFP cathodes is around 6.5% [24], suggesting that LFP experiences less strain during (de)lithiation, and they generally show improved cycle life compared to NMC cells, which might explain the lack of deformations.

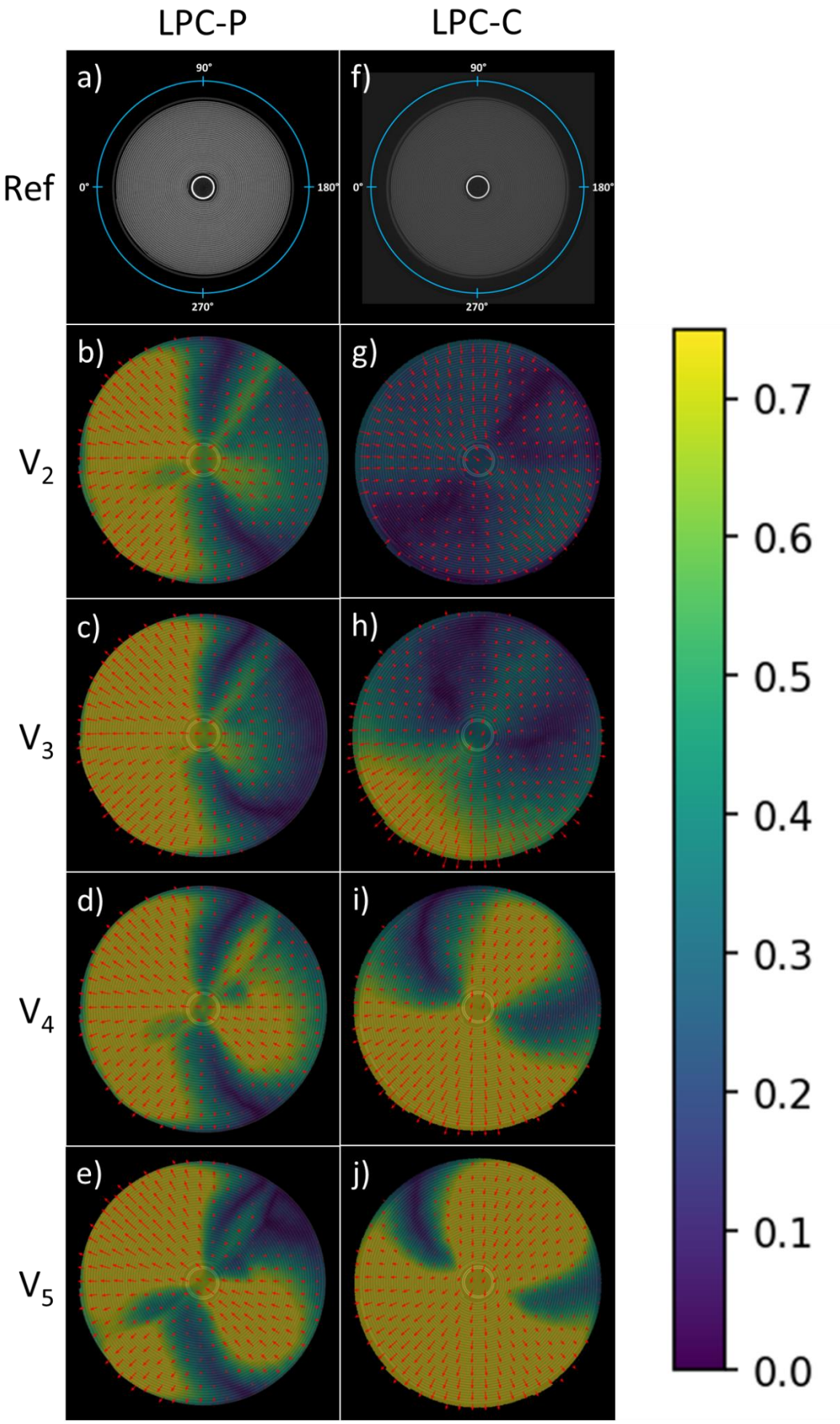

Figure 7: MERt of the pristine and cycled LPC cells, (a-e) LPC-P, (f-j) LPC-C.

3.2 Virtual Unrolling

Virtual unrolling is carried out on the X-ray data of the pristine and cycled cells used in this study. The X-ray dataset is oriented such that the outer current collecting tab (if present) is always be located around 270° for ease of interpretation. The orientation of the unrolling figures is the same as the orientation shown in the reference images shown in Figure 3–Figure 7 and one can use the angular co-ordinates provided in the reference images to locate features in the unrolling figure. The unrolled figures can be seen in Figure 8, where the *x-axis* denotes the angular coordinates in the cell and the *y-axis* denotes the radial coordinates. Essentially, once the coordinates of the repeating layer is identified, as outlined in the methodology, each repeating layer that is between 0° to 360° is plotted from the outside-in (outer layers towards the top of the unrolling figures, and the inner layers towards the bottom). Blue boxes have been used to indicate the location of the outer tabs in the unrolling figures, same as in the reference images, and the gaps in the middle of the repeating layers in the unrolling figures denotes the presence of an internal current collecting tab. In the unrolling figures for the pristine cells, pre-existing inflections in the jelly roll can be seen. These appear as crimps or curves of varying size along the electrode layers. When comparing the location of the flow fields overlaid on the frames of the motion enhanced videos of the pristine cells generated by MERt in Figure 3–Figure 7 to their counterparts in the unrolled figures in the Figure 8, it can be seen that the inwards forces are occurring at and around such pre-existing inflections as predicted by Kok *et al.* [2]. For example, it can be seen that VTC6-*P* contains two shallow inflections around 120° and 330°, and from Figure 5c-d it can be seen that compressive forces are acting around those locations. Another observation is that some of the inflections and compressive forces are located where the electrode roll ends at the inner core. Whereas other parts of the electrode roll are semi-secured in place due to the tight packing of the electrode rolls, the positive electrode end is relatively unsecured. This is also demonstrated by the shift in the electrode in the inner core in some of the enhanced videos, implying that the electrodes are *'unwinding'* from the inside. Thus, it is the location at which the least amount of force would be required to *'buckle'* the electrodes.

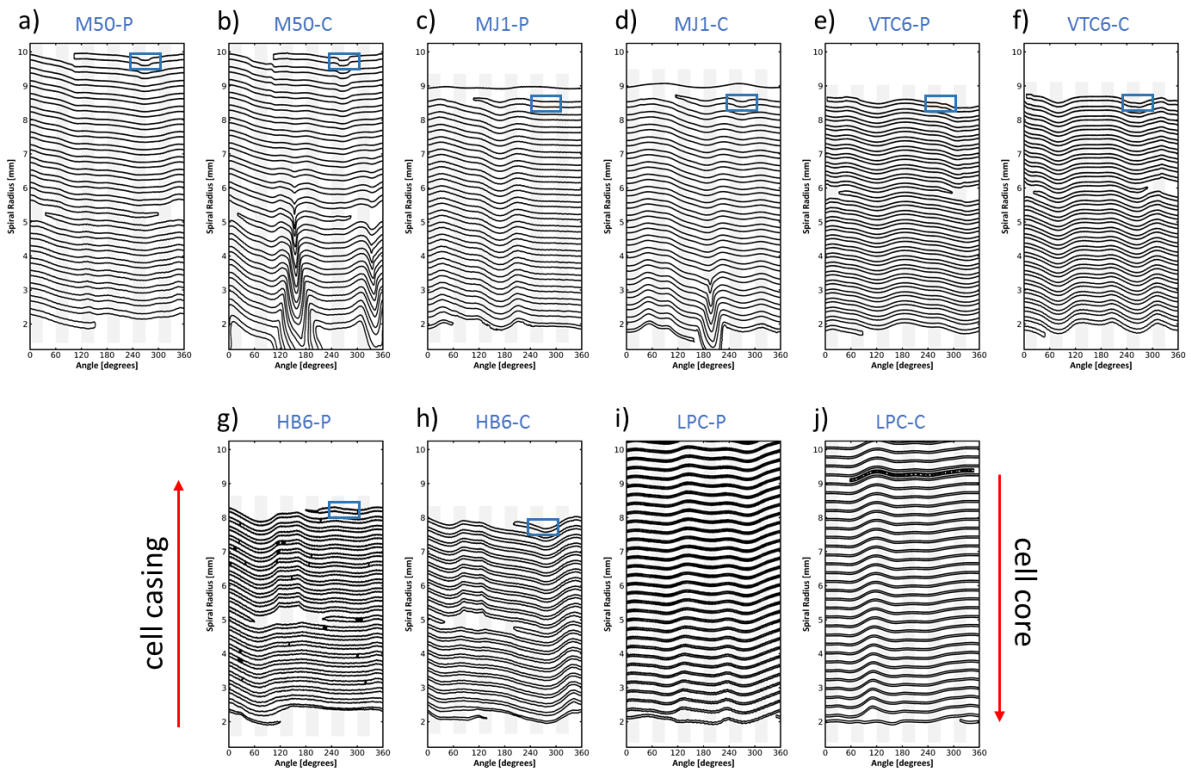

Figure 8: Virtually unrolled electrodes of (a-b) M50-P and M50-C, (c-d) MJ1-P and MJ1-C, (e-f) VTC6-P and VTC6-C, (g-h) HB6-P and HB6-C, and (i-j) LPC-P and LPC-C, respectively. Blue box indicates the location of the outer current collecting tab, if present.

As discussed previously, for cycled cells where visible deformations exist, the compressive forces act at those locations and around them. For the cycled cells that do not contain any visible deformations, virtual unrolling shows that they still contain inflections in their jelly roll that cannot be easily identified. The VTC6-*C* contains inflections at two points in the jelly roll, one around 90° and one around 270°. It can be seen from Figure 5g-j that whereas a compressive force acts at and around 90° first, a compressive force develops around 270° from V_4 onwards with a smaller magnitude. Unlike the other cells, in the unrolling figure for HB6-*C* shows an upwards inflection at around 360°, as opposed to a downwards inflection. The compressive force is acting around that location, however, there is nothing in the unrolling figure to indicate why there might be such a defined split between the compressive force and the expansive force. The LPC-*C* cell shows a similar behaviour of a split between a compressive force around the inflection at 120° and an expansive force at the opposite direction that cannot be explained by the unrolling figure.

It can be seen from the unrolling figures, that in some cases, there are inflection points located at 270°, in line with where the tab is located (if present), however it is not the case for all cells. Similarly, the inner, positive

current collecting tab is identified by a disconnect in the electrode layer in the unrolling figure, and in a similar fashion, it does not always correlate to an inflection point along the angular coordinate at which the tab is located. Therefore, the exact influence of the current collecting tabs on the jelly roll is hard to identify.

All cells contain variances, as clearly shown by the differences in the VTC6 cells and the HB6 cells in Figure 5 & Figure 6, respectively. These differences arise during the manufacturing process and lead to slight differences in the physical locations of cell internal features, such as current collecting tabs. This in turn leads to the differences in inflection points in the jelly roll and in the nucleation points of electrode shifts and deformations, which accounts for some of the variances seen in the flow fields produced by MERt of these cells. Furthermore, the observed change in the physical shape of the cells during a charge cycle due to the expansion of the cell housing and the application of an automated alignment tool causes minor artefacts in the videos, accounting for potential artefacts in the flow fields. This is a point of interest for future works as mentioned in the *Conclusions and Future Work* section.

Conclusions and Future Work

We have used a combination of a video motion enhancement technique to magnify the motion of electrodes during the lithiation process and an image registration technique based on optical flow in the analysis of batteries for the first time. The motion enhancement and registration technique, MERt, was carried out on five cell types by obtaining X-ray data at various steps in the charge cycle and converting slices from each dataset into videos. It was clearly observed that the shift of electrodes caused by the lithiation process towards the cell core is occurring at pre-existing inflection points in the jelly roll, as revealed by virtual unrolling. Virtual unrolling also revealed that location of the inflection in the jelly roll might be influenced by the location at which the electrode roll ends at the center of the cell. For cycled cells already containing large electrode deformations, the shift was concentrated around the deformations, which is believed to contribute to the expansion of the deformations. It was also seen that the cells without large deformations showed a greater expansion of electrodes towards the outer casing, indicating that once the electrode buckles, it provides a point of weakness there the compressive forces can concentrate.

Differences in the location of internal structures such as the location of the current collecting tabs was observed between cells of the same model and batch. This difference seems to have caused differences in the flow fields between the cells, however, there isn’t enough information to elucidate the exact effect of the differing internal structures.

We have attempted to briefly, and systematically categorise the behaviour of the cells and their cause as observed through video enhancement and optical field flows, as shown in Table 3.

Table 3: Observed changes in the cells in this study.

Battery	Feature	Effect
M50	Positive tab	Supresses some outward flow of electrodes.
	Negative tab	Provides space for electrode expansion along edges.
	Positive electrode end	Where deformation initiates and the focal point of compressive electrode flow.
	Deformation	Causes increased stress alongside the point of deformation
MJ1	Negative tab	Provides space for electrode expansion along edges.
	Positive electrode end	Where deformation initiates and the focal point of compressive electrode flow.
	Deformation	Causes increased stress alongside the point of deformation
VTC6	Positive tab	No observable effect.
	Inner negative tab	Supresses some inward flow of electrodes.
	Outer negative tab	Provides space for electrode expansion along edges.
	Positive electrode end	The focal point of compressive electrode flow.
	Mandrel	Supresses some inward flow of electrodes.
HB6	Positive tab	No observable effect.
	Inner negative tab	Supresses some inward flow of electrodes, along with the outer negative tab, forms a line of dead zone for most of the charge cycle.
	Outer negative tab	Supresses some outward flow of electrodes, and provides space for electrode expansion along edges.
	Positive electrode end	The focal point of compressive electrode flow for the pristine cell, not for the cycled cell.
LPC	Positive electrode end	Some compressive electrode flow for the pristine cell, but not the focal point, and the focal point of compressive electrode flow for the cycled cell.
	Mandrel	Supresses some inward flow of electrodes, and might be creating dead zones at points in the cell by dividing the inward and outward flow.

From the observed trends in Table 3, it could be concluded that the biggest driving factor for the eventual deformation of the cells is the location of the positive electrode end at the centre of the cell. In the case of the pristine HB6 cell (HB6-*P*) not following that trend: it contains a significant inflection point at where the focal point of the inwards compressive force is located. Hence it might be argued that deformation occurs at the first instance at a point of significant pre-existing inflection point (which in a lot of cases is located besides the positive electrode end), and lacking an inflection point acting as a nucleation point, deformation occurs at the positive electrode end. In the case of the LPC cell, there may be factors affecting its behaviour from beyond the region of interest, such as the numerous current collecting tabs.

The possible casing deformation behaviour observed makes it more difficult to align the slices of the various scans during the charge phase, potentially introducing minor artefacts in the flow fields presented. Work in the future will focus on more on investigating the casing deformation and attempting to quantify the casing expansion, as

well as improving the alignment process. The formation of a 3D delamination framework through meshes of high-resolution scans of the full length and width of a cell at different points in its cycle life is also desirable.

Lithium-ion batteries are currently the most promising energy conversion devices for utilisation in electric vehicles, however, there are still challenges in fully understanding the mechanisms that drive degradation and in optimising cell design. Here, we have presented a combined approach to investigate one of the mechanisms behind cell degradation – cell deformation and electrode cracking/delamination caused by the expansion and contraction of electrodes during (de)lithiation. Utilising a method to enhance the electrode displacement that occurs during cell charging with an image registration process to create a motion enhancement and registration technique, we were able to identify displacement *'hotbeds'* in pristine cells and correlate them with observed deformations in cycled cells (if present) and also provide some information on the influence of the cell internal design on electrode displacement. We believe this technique, MERt, can be used in instances such as mapping the macro electrode displacement in prototype cells to inform cell design an minimise cell deformations in the long run. We were not able to test a wide array of cells, nor a large number of cells in this study, however, manufacturers would have the capacity to test a large number of cells to obtain a more statistically robust displacement map of a cell model.

Acknowledgements

This work was carried out with funding from the Faraday Institution (faraday.ac.uk; EP/S003053/1), grant number FIRG003, FIRG0025, FIRG0028; and the EPSRC grant EP/R020973/1. PRS would like to acknowledge the Royal Academy of Engineering (CiET1718\59) for financial support.

References

[1] T. Waldmann, S. Gorse, T. Samtleben, G. Schneider, V. Knoblauch, and M. Wohlfahrt-Mehrens, "A Mechanical Aging Mechanism in Lithium-Ion Batteries," *J. Electrochem. Soc.*, vol. 161, no. 10, pp. A1742–A1747, 2014.

[2] M. D. R. Kok *et al.*, "Virtual unrolling of spirally-wound lithium-ion cells for correlative degradation studies and predictive fault detection," *Sustain. Energy Fuels*, vol. 3, no. 11, pp. 2972–2976, 2019.

[3] Y. Qi, H. Guo, L. G. Hector, and A. Timmons, "Threefold Increase in the Young's Modulus of Graphite Negative Electrode during Lithium Intercalation," *J. Electrochem. Soc.*, vol. 157, no. 5, p. A558, 2010.

[4] O. O. Taiwo *et al.*, "Microstructural degradation of silicon electrodes during lithiation observed via operando X-ray tomographic imaging," *J. Power Sources*, vol. 342, pp. 904–912, 2017.

[5] A. J. Louli, J. Li, S. Trussler, C. R. Fell, and J. R. Dahn, "Volume, Pressure and Thickness Evolution of Li-Ion Pouch Cells with Silicon-Composite Negative Electrodes," *J. Electrochem. Soc.*, vol. 164, no. 12, pp. A2689–A2696, 2017.

[6] S. C. Yin, Y. H. Rho, I. Swainson, and L. F. Nazar, "X-ray/neutron diffraction and electrochemical studies of lithium De/Re-intercalation in Li1-xCo1/3Ni1/3Mn 1/3O2 (x = 0 → 1)," *Chem. Mater.*, vol. 18, no. 7, pp. 1901–1910, 2006.

[7] E. Markervich, G. Salitra, M. D. Levi, and D. Aurbach, "Capacity fading of lithiated graphite electrodes studied by a combination of electroanalytical methods, Raman spectroscopy and SEM," *J. Power Sources*, vol. 146, no. 1–2, pp. 146–150, 2005.

[8] H. Liu *et al.*, "Intergranular Cracking as a Major Cause of Long-Term Capacity Fading of Layered Cathodes," *Nano Lett.*, vol. 17, no. 6, pp. 3452–3457, 2017.

[9] S. R. Stock, "Recent advances in X-ray microtomography applied to materials," *Int. Mater. Rev.*, vol. 53, no. 3, pp. 129–181, 2008.

[10] D. S. Eastwood *et al.*, "Lithiation-induced dilation mapping in a lithium-ion battery electrode by 3D X-ray microscopy and digital volume correlation," *Adv. Energy Mater.*, vol. 4, no. 4, pp. 1–7, 2014.

[11] D. P. Finegan *et al.*, "Quantifying bulk electrode strain and material displacement within lithium batteries via high-speed operando tomography and digital volume correlation," *Adv. Sci.*, vol. 3, no. 3, pp. 1–11, 2015.

[12] B. K. P. Horn and B. G. Schunck, "Determining optical flow," *Artif. Intell.*, vol. 17, no. 1–3, pp. 185–203, 1981.

[13] J. Schindelin *et al.*, "Fiji: an open-source platform for biological-image analysis," *Nat. Methods*, vol. 9, no. 7, pp. 676–682, Jul. 2012.

[14] N. Wadhwa, M. Rubinstein, F. Durand, and W. T. Freeman, "Phase-based video motion processing," *ACM Trans. Graph.*, vol. 32, no. 4, 2013.

[15] H. Y. Wu, M. Rubinstein, E. Shih, J. Guttag, F. Durand, and W. Freeman, "Eulerian video magnification for revealing subtle changes in the world," *ACM Trans. Graph.*, vol. 31, no. 4, 2012.

[16] S. van der Walt *et al.*, "scikit-image: image processing in Python," *PeerJ*, vol. 2, no. 1, p. e453, Jun. 2014.

[17] C. Zach, T. Pock, and H. Bischof, "A Duality Based Approach for Realtime TV-L 1 Optical Flow," in *Pattern Recognition*, vol. 0, no. x, Berlin, Heidelberg: Springer Berlin Heidelberg, 2007, pp. 214–223.

[18] A. Wedel, T. Pock, C. Zach, H. Bischof, and D. Cremers, "An Improved Algorithm for TV-L 1 Optical Flow," in *Lecture Notes in Computer Science (including subseries Lecture Notes in Artificial Intelligence and Lecture Notes in Bioinformatics)*, vol. 5604 LNCS, 2009, pp. 23–45.

[19] J. Sánchez Pérez, E. Meinhardt-Llopis, and G. Facciolo, "TV-L1 Optical Flow Estimation," *Image Process. Line*, vol. 3, no. 1, pp. 137–150, Jul. 2013.

[20] W. E. Lorensen and H. E. Cline, "Marching cubes: A high resolution 3D surface construction

algorithm," in *Proceedings of the 14th annual conference on Computer graphics and interactive techniques - SIGGRAPH '87*, 1987, vol. 21, no. 4, pp. 163–169.

[21] A. N. P. Radhakrishnan, M. Pradas, E. Sorensen, S. Kalliadasis, and A. Gavriilidis, "Hydrodynamic Characterization of Phase Separation in Devices with Microfabricated Capillaries," *Langmuir*, vol. 35, no. 25, pp. 8199–8209, Jun. 2019.

[22] P.-E. Danielsson and O. Seger, "Generalized and Separable Sobel Operators," in *Machine Vision for Three-Dimensional Scenes*, H. Freeman, Ed. Academic Press, Inc., 1990, pp. 347–379.

[23] L. K. Willenberg, P. Dechent, G. Fuchs, D. U. Sauer, and E. Figgemeier, "High-precision monitoring of volume change of commercial lithium-ion batteries by using strain gauges," *Sustain.*, vol. 12, no. 2, 2020.

[24] M. Nishijima *et al.*, "Accelerated discovery of cathode materials with prolonged cycle life for lithium-ion battery," *Nat. Commun.*, vol. 5, pp. 1–7, 2014.